Examination of the cerium α-ε phase transition under dynamic loading with x-ray diffraction

M. T. Beason and B. J. Jensen
Los Alamos National Laboratory, Los Alamos, New Mexico 87545, USA

(Received 3 February 2022; revised 4 May 2022; accepted 9 June 2022; published 16 June 2022)

Recent examination of the cerium Hugoniot with pyrometry and x-ray diffraction (XRD) has revealed a narrow solid-liquid two-phase region. It has been suggested that nonequilibrium melting may be occurring along the Ce Hugoniot, with either melt kinetics or a sluggish α-ε transition impeding the transition. In particular, the kinetics of the α-ε is unknown and the location of the phase boundary is in dispute. Static measurements suggest a nearly vertical phase boundary that intersects the Hugoniot at 6–7 GPa. This lies in direct conflict with dynamic measurements along the Hugoniot observing α-Ce through incipient melt. This work presents dynamic experiments using XRD to examine the behavior of the α-ε phase transition. The results show that the α-ε phase transition occurs through a tetragonal distortion, with the transition beginning at temperatures below the solid Hugoniot. Following the initial deviation from an ideal fcc structure, the c/a ratio is found to gradually increase with no steady value observed in the ε phase within the range of these experiments (below 17 GPa). Multiple diffraction patterns captured during the peak stress state show no significant change in c/a ratio prior to uniaxial release, upon which Ce reverts to an fcc structure. The results indicate that the α-ε transition occurs rapidly, both on loading and release. An examination of the c/a ratio with increasing temperatures suggests 11.5 GPa as a lower bound for the location of the α-ε-liquid triple point.

DOI: 10.1103/PhysRevB.105.214107

I. INTRODUCTION

Cerium (Ce) is the first element in the periodic table with an f-shell electron at ambient conditions. As such, it serves as a prototype for understanding how f-shell electrons behave under extreme pressures (P) and temperatures (T) with numerous studies having sought to understand the Ce phase diagram (Fig. 1) [1–18]. The majority of work has focused on the isostructural γ-α (fcc, $Fm\bar{3}m$) phase transition [6,7,19,20], melt boundary [1–4,11–13], or room temperature (RT) compressibility [14,15]. Recently, there has been significant interest in understanding the behavior of Ce at elevated T and P [5–11]. These efforts have constrained the location of the γ-α critical point [6,7], and the two-phase region along the Hugoniot [1–3].

Recent studies of shock melting in Ce have suggested a narrow solid-liquid two-phase region along the Hugoniot. Two separate studies using pyrometry to infer the temperature along the Hugoniot have found little deviation in the P-T Hugoniot through the melting transition [2,11]. Jensen *et al.* [2] used sound speed measurements to separate temperatures along the solid portion of the Hugoniot from the liquid portion of the Hugoniot. Once fit, the solid-liquid two-phase region was found to occur from, nominally, 10 to 12 GPa. Alternatively, Hixson *et al.* [11] found that their temperature data was best fit by a straight line, with no definitive melt curve observable. This result motivated a discussion where it was suggested that either the enthalpy of fusion is less than previously expected or that shock melting in Ce is inhibited by sluggish kinetics associated with melting or the α-ε (bct, $I4/mmm$) phase transition. The two interpretations are fundamentally about whether Ce follows a nominally equilibrium Hugoniot (small enthalpy of fusions) or deviates to a nonequilibrium path near melt (sluggish kinetics).

In a previous publication, the authors examined shock melting and the solid-liquid two-phase region of the Ce Hugoniot using time-resolved x-ray diffraction (XRD) [1]. It was shown that Ce remains fcc along the solid Hugoniot through incipient melt with no significant crystalline phase observed beyond 12 GPa. With this information the bulk and longitudinal sound speeds were reinterpreted and it was found that melt completion occurs at 12–14 GPa. Time-resolved diffraction patterns showed no evidence of a crystalline superheated solid and steady diffraction patterns were observed for over 400–500 ns after impact. Based on the lack of any observable kinetic response on timescales beyond $\sim$10 ns, it was concluded that melting occurs rapidly along the Ce Hugoniot with the solidus being located near 10.4 GPa and the liquidus at 12–14 GPa. This interpretation is consistent with a small enthalpy of fusion and a narrow two-phase region, as suggested by Jensen *et al.* [2]. If Ce were to shock into a superheated state lasting hundreds of nanoseconds it would be expected to exhibit strong fcc diffraction peaks over the timescale of our previous experiments. These previous results are not compatible with melting kinetics being slow.

While the melting kinetics in Ce has been shown to be relatively fast, the kinetics of the α-ε transition has not been fully explored. Though it is not clear that a mixture of α and ε would explain the diffraction measurements along the Hugoniot or even delay melting (there is no requirement that α transition to ε prior to melting), an accurate understanding of the α-ε transition is a necessary piece of constructing the

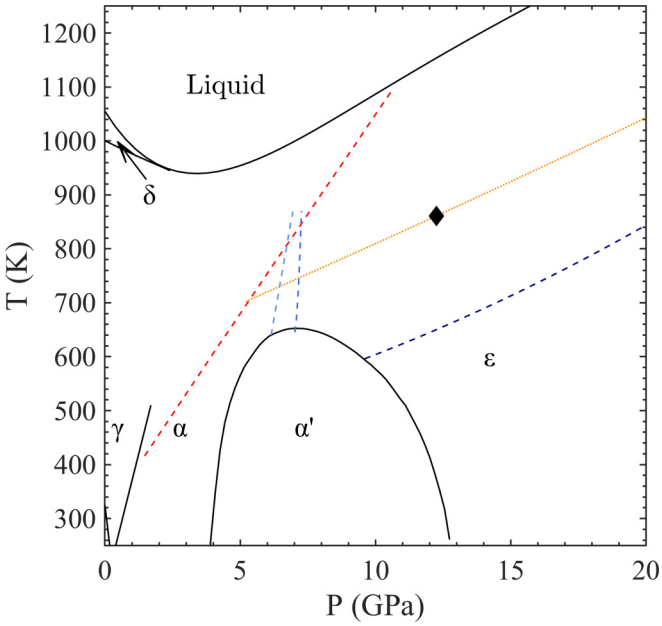

FIG. 1. The current state of the Ce phase diagram with the solid *P-T* Hugoniot (red dashed), proposed α-ε phase boundaries based on static data (light blue [9], blue [10], dark blue [16]), and the point (black diamond) along the 5.2 GPa secondary Hugoniot (orange) where the compression can no longer be explained by an α-Ce equation of state.

equilibrium phase diagram (Fig. 1). Following examination of the 773 K isotherm and 5.2 GPa secondary Hugoniot, it was found that a two-phase (α-ε) equation of state (EOS) was necessary to fit the observed second shock arrival times beyond 12.25 GPa [8]. Along the 773 K isotherm, Ce was identifiable as fcc prior to 6 GPa and ε beyond 12 GPa; however, the intermediate region was indeterminate. Several measurements of the α-ε phase boundary have been reported [9,10,16]. In particular, the boundaries of Munro *et al.* [9] and Schiwek *et al.* [10] extend almost vertically from the α' dome and intersect the solid Hugoniot near 7 GPa. As mentioned above, this transition is not observed along the principal Hugoniot; however, significant transition kinetics in a first order α-ε transition may explain the transition being delayed until 12.25 GPa on the secondary Hugoniot and not being observed along the principal Hugoniot through 10 GPa.

The results of Munro *et al.* [9] suggest an entirely different view of the α-ε transitions. When examined along isotherms between 600 and 770 K, the α-ε transition was found to occur with negligible volume change. The continuous transition occurs as *c/a* (see Fig. 2) gradually increases from an ideal fcc value ($\sqrt{2}$) to nominally 1.5. Such a transition does not exhibit a traditional mixed-phase region, where separate fcc and bct phase are observable in XRD and an isentrope would trace a phase boundary in *P-T* space (i.e., there is no associated transition enthalpy). Identifying such a transition under dynamic loading based on continuum measurements (velocimetry or pyrometry) alone would be difficult. Continuum diagnostics, such as velocimetry, are used to identify phase transitions through an associated volume collapse or change in compressibility along a defined path (Hugoniot or

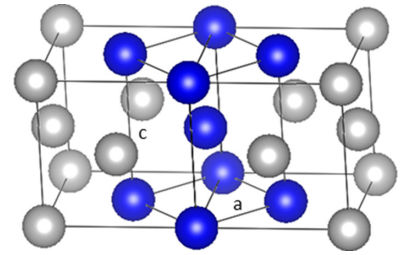

FIG. 2. Wireframe representation [21] of two fcc unit cells (gray and blue atoms) with the equivalent bct unit cell highlighted in blue.

isentrope). A phase transition exhibiting a negligible volume collapse or change in shock velocity would be nearly unobservable through velocimetry alone. In this case, XRD may be required to experimentally constrain the transition onset.

This work uses XRD collected on multishock loaded Ce to constrain the location of the α-ε phase boundary. The Ce was initially shocked to stresses above the γ-α collapse, but prior to incipient melt, before reaching a steady stress state at longitudinal stresses (σ) from 8 to 17 GPa. This allowed the Ce phase diagram to be examined at temperatures above the α' dome and below the melt boundary. These experiments, along with previous observations near the Hugoniot, constrain the α-ε phase boundary to fall at temperatures below the Hugoniot. No kinetics is observed on the timescale of these experiments. Instead, the α-ε transition occurs through an increase in *c/a* ratio under dynamic loading. The *c/a* ratio is observed to rapidly increase from $\sqrt{2}$ to 1.48 before gradually increasing with pressure. The α-ε phase boundary does not intersect the solid region of the Hugoniot when observed under dynamic loading. It is found to have a positive slope that is shallower than the boundaries of Schiwek *et al.* [10] or Munro *et al.* [9] and is not anticipated to intersect the melt boundary below 11.5 GPa.

II. EXPERIMENTAL METHODS

The Ce samples used in this work were processed to be fine grained (nominally 50 μm) γ-Ce. The initial material was 99.99% pure on a metals basis with an initial density of 6.687 g/cm^3 and ambient longitudinal and shear-wave speed of 2.339 and 1.326 km/s, respectively [3]. The Ce was lapped to a nominal thickness of 75 μm after being adhered to a 1.6 mm thick (100) LiF window. The Ce samples were impacted by multilayered flyers, Fig. 2(a), launched with the gas gun at sector 35-ID-E of the Advanced Photon Source (APS, Argonne, IL). The front layer of the flyer was a thin (60–120 μm) polymer (Kel-F, PMMA, polystyrene, or TPX) with the second layer being 3 mm of either LiF or one of the listed polymers with a higher shock impedance than the front layer. The impact velocity (v_f), determined through a series of optical breaks at known distances, allows the initial impact state to be determined through impedance matching [22]. Photonic Doppler velocimetry (PDV) [23] was used to measure the motion of the Ce LiF interface, enabling validation of the impedance match solutions and allowing the arrival of the release wave to be observed.

The diffraction measurements were taken during 24-bunch mode operation of the APS, providing a series of x-ray singlets nominally 33.5 ps in width at 153.4 ns intervals. The output of a 2.7 cm undulator (U27) was shaped to produce the energy spectrum presented in Fig. 2(b) and used to produce a diffraction pattern captured using a 4-frame detector described elsewhere [24]. A diffraction image of a thin Si standard was taken prior to every experiment, allowing the detector position to be calibrated in GSAS-II [25]. Detector ghosting was corrected for by subtracting a scaled fraction of the previous frame.

III. RESULTS AND ANALYSIS

Previous work has shown that the Ce Hugoniot remains fcc through 10 GPa with no evidence of crystalline peaks above 12 GPa [1]. Therefore, it is necessary to utilize multiple shocks to examine the α-ε phase diagram. Shocking to the same P in two or multiple steps generates less entropy compared to a single shock to the same P, resulting in a lower T state. Plate impact experiments often utilize a double shock configuration where the sample is either part of a two-layer flyer impacting a velocimetry window or impacted by a flyer composed of two different impedances. This allows precise measurement of a secondary Hugoniot, a locus of shock states originating at a nonambient state along the principal Hugoniot. If the α-ε transition exhibits slow transition kinetics, this should be directly observable in XRD.

When diffraction measurements are taken in a transmission geometry it is necessary to minimize the overall absorption of the impactor, sample, and window to maximize the diffraction signal. This complicates standard double shock experiments, which typically use a thick sample geometry and high density impactors to reach a well-defined state. Here, a multishock loading scheme has been used that is approximately a double shock experiment. The impedance matching diagram in Fig. 3(a) illustrates the notional loading path for Ce impacted with a LiF/Kel-F flyer plate at 1.3 km/s. Impacting a thin layer of Ce with a multilayer impactor provides two clearly defined stress states to be reached. The first shock state (1) is determined by the intersection of the left-facing Kel-F Hugoniot [26] centered at v_f with the right-facing Ce Hugoniot [3]. Breakout of this shock brings the Ce-LiF interface to state (1′). The second shock is generated when a shock originating at the impact face propagates upstream through the Kel-F and reaches LiF impactor. This shock then drives the Ce to state (2). A series of small reverberations follows, bringing the Ce and Kel-F to the final ring state (r), which is determined by the intersection of the LiF window with the high impedance impactor layer (LiF in this example). Strictly speaking, state (r) lies between a secondary Hugoniot centered at (1) and the isentrope extending from (1); however, only small reverberations are required to bring the Ce from (2) to (r), with loading occurring primarily in two shocks. As such, in the following discussion the loading paths will be referred to as secondary Hugoniots.

The Ce-LiF interface velocity for experiment 19-4-046, presented in Fig. 4(b), is found to closely correspond to the impedance matching solution. State (1′) is observed as a brief plateau prior to the arrival of the second shock state with

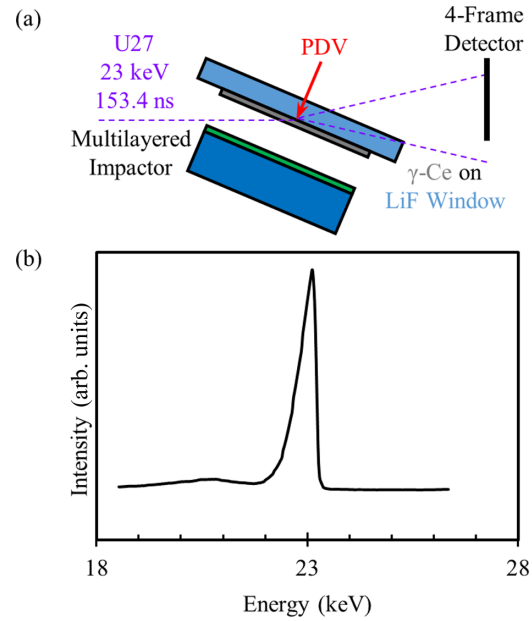

FIG. 3. (a) Experimental geometry. (b) Energy spectrum used in diffraction measurements.

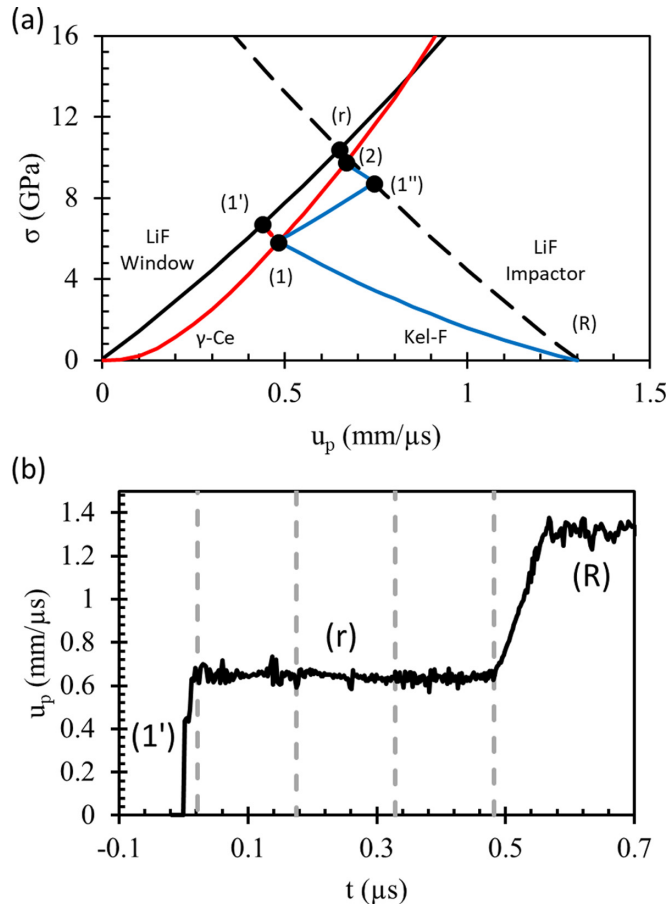

FIG. 4. (a) Impedance matching diagram for a LiF (dashed black) and Kel-F (solid blue) impactor striking Ce (red) with a LiF window (solid black). (b) Measured Ce-LiF interface velocity with corresponding states and time of arrival of the x-ray pulses (dashed gray lines) labeled.

TABLE I. Summary of experimental parameters measured and determined through velocimetry and calculated temperatures.

Shot	Impactor	t_p (μm)	t_{Ce} (μm)	t_w (mm)	v_f (km/s)	$u_{p,1}$ (km/s)	σ_1 (GPa)	$u_{p,2}$ (km/s)	σ_2 (GPa)	T_2 (K)
19-4-045	LiF/TPX	105(3)	69(3)	1.680	1.963	0.469	5.55	0.978(10)	16.8(2)	913
19-4-046	LiF/Kel-F	116(3)	69(3)	1.567	1.310	0.503	6.23	0.652(12)	10.4(2)	835
19-4-047	LiF/PMMA	91(3)	89(3)	1.587	1.545	0.523	6.64	0.790(20)	13.0 (4)	910
19-4-048	LiF/TPX	101(3)	79(3)	1.592	1.465	0.407	4.37	0.736(7)	12.0(1)	792
19-4-049	LiF/Kel-F	96(3)	77(3)	1.588	1.824	0.670	9.83	0.915(16)	15.5(3)	1136
19-4-050	LiF/Kel-F	56(3)	78(3)	1.594	1.589	–	–	0.794(5)	13.1(1)	1001
19-4-051	LiF/Kel-F	60(5)	93(3)	1.577	1.173	0.408	4.38	0.588(5)	9.3(1)	726
19-4-052	LiF/PMMA	75(3)	77(3)	1.574	1.168	0.419	4.61	0.581(6)	9.2(1)	736
19-4-053	LiF/TPX	102(3)	63(3)	1.604	1.561	0.361	3.54	0.781(5)	12.9(1)	780
21-4-016	PMMA/TPX	120(5)	67(3)	1.519	2.112	0.515	6.47	0.583(9)	9.2(2)	856
21-4-017	PMMA/TPX	120(5)	65(3)	1.533	2.195	0.499	6.16	0.616(12)	9.8(2)	932
21-4-018	PMMA/PS	120(5)	60(3)	1.452	1.992	0.558	7.38	0.544(17)	8.5(3)	905
21-4-019	PMMA/PS	120(5)	61(3)	1.504	1.504	0.662	9.65	0.669(8)	10.8(1)	1030

the arrival of the second shock followed by small amplitude oscillations leading to state (r). Approximately 0.5 μs after the first shock arrives at the Ce-LiF interface, a rarefaction fan centered at the upstream side of the LiF window accelerates the sample as the Ce is brought to ambient P. A series of four diffraction images (denoted by dashed gray lines) is captured between the arrival of the second shock and the rarefaction. A summary of relevant experimental parameters including measured thicknesses (t), impact velocity (v_f), and particle velocities (u_p) as well as σ determined through impedance matching is provided in Table I.

Steady diffraction patterns were observed at all times between the arrival of the second shock and the rarefaction fan. An example of this is presented in Fig. 5, where the sample shocks are observed to exhibit a similar diffraction pattern at 34 and 341 ns after shock breakout. This indicates that the α-ε transition either has rapid kinetics, or transitions over a significantly longer timescale than a typical dynamic experiment. The lack of observable kinetics allowed the integrated patterns to be averaged over this time period. The resulting diffraction patterns are presented in Fig. 6, along with patterns taken at states centered at the same nominal Hugoniot stress previously presented in [1]. A scaled ambient diffraction pattern (green) has been provided for reference and is followed by patterns taken with an initial shock state (1) of nominally 4 GPa (blue), 5.6 GPa (red), 7 GPa (magenta), and 9 GPa (yellow). The patterns have been fit using a summation of pseudo-Voigt peaks with different wavelengths normalized by the intensities presented in Fig. 2(b) in order to determine the corresponding d spacings. The resulting curves (black dashed curves) overlay the captured diffraction patterns.

Along a given secondary Hugoniot (i.e., within an individual color set), the spacing between the primary diffraction peak and the second strongest diffraction peak increases with pressure. This is accompanied by splitting of the (200), (220), and (311) fcc diffraction peaks into the (002), (110); (112), (200); and (103), (211) bct diffraction peaks, respectively. This splitting is most evident in the measured d spacings (hollow symbols) presented in Fig. 7(a). The measured d spacings were indexed to a bct structure ($I4/mmm$) and a least-squares fit was used to determine lattice parameters c and a (see Fig. 2). The d spacings resulting from this indexing (i.e., the determination of lattice parameters c and a from the measured d spacings) are plotted as pluses in Fig. 7(a) for comparison. Reasonable agreement can be observed, with the largest uncertainty found in the (002) d spacings, which stems from

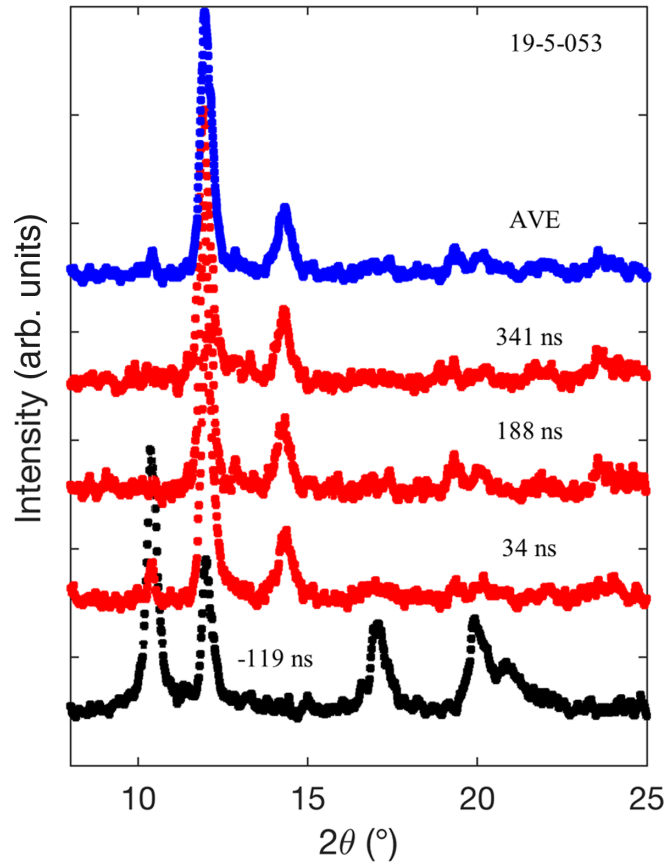

FIG. 5. Time-resolved diffraction patterns for experiment 19-5-053. A steady diffraction pattern is observed over the duration of the 12.9 GPa hold state (red). The average of the hold state (blue) was determined to increase the signal to noise ratio for the final indexed data.

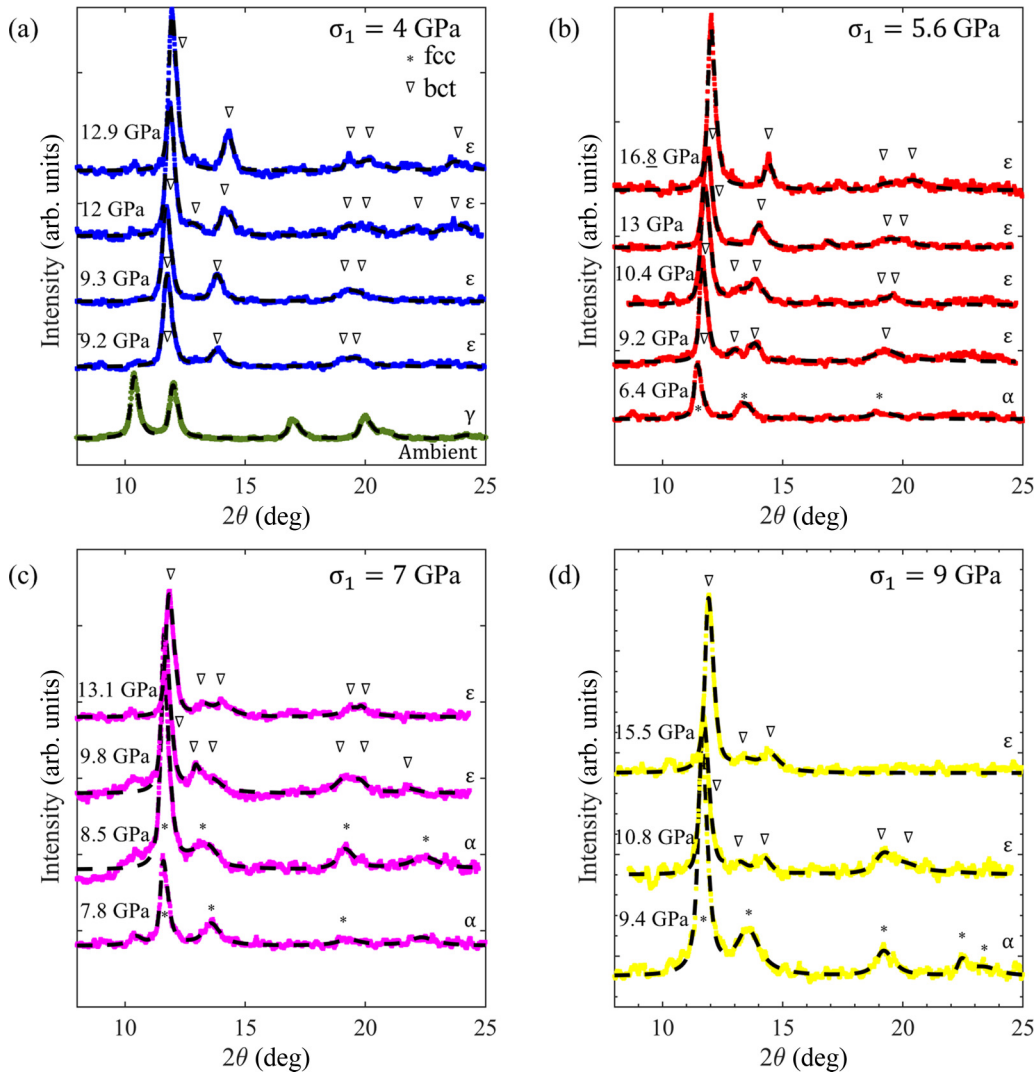

FIG. 6. Waterfall plot with diffraction patterns taken at ambient (green) and following the ring up from initial shock states at (a) 4 GPa (blue), (b) 5.6 GPa (red), (c) 7 GPa (magenta), and (d) 9 GPa (yellow). The patterns have been fit (black dashed lines) with a polynomial baseline and a summation of pseudo-Voigt peaks. The patterns are indexed according to the ascribed phase, with no clear evidence of α-ε coexistence. The patterns at the lowest stress for the red, magenta, and yellow series are from [1].

the low signal to noise ratio for that diffraction peak. Once determined, a and c were used to calculate the atomic volume (Ω) and linear strain along the a axis ($\epsilon_a = 1-a/a_0$) and c axis ($\epsilon_c = 1 - c/c_0$); c_0 and a_0 are the bct-equivalent ambient lattice parameters for γ-Ce. Measurements of Ω are provided in Fig. 7(b), with ϵ_a and ϵ_c compared with the isotropic linear strain [$\epsilon_{iso} = (1 - \Omega/\Omega_0)/3$] for data collected in this work as well as the 5.2 GPa secondary Hugoniot from [8] presented in Fig. 7(c). Note that ϵ_a and ϵ_c are nearly equal to ϵ_{iso} in an fcc lattice as opposed to the bct lattice, where $\epsilon_c < \epsilon_{iso} < \epsilon_a$. Measurements of the a, c, c/a, and Ω are provided in Table II.

Several metals have been identified as having high pressure phases that are metastable following release to ambient pressure. The ω phases of Zr and Ti are particularly noteworthy for persisting long after release and recovery [27,28]. Recovery experiments are capable of observing phases that require extended periods of time (i.e., days or more) to revert to the ambient phase, but are unable to observe transitions that complete over shorter timescales. Alternatively, velocimetry provides a means of observing transition kinetics that occurs on the nanosecond timescale [29]. It is difficult to determine when a phase transition occurs over intermediate timescales. Time-resolved diffraction provides a means to examine the phase immediately following release (i.e., ~0.1–1 μs).

To observe whether the α-ε transition exhibits any observable delay in reversion to an fcc structure, a sample was shocked into ε phase space and probed through release to ambient pressure (experiment 19-4-045). The time-resolved diffraction patterns captured in this experiment are presented in Fig. 8. In this plot, the (101) and (110) ε peaks are observable while the sample is at 16.8 GPa (376 ns after shock breakout). A diffraction pattern captured midrelease (530 ns) exhibits three peaks, with the first peak being broad and rounded, as would be expected for diffraction from a distribution of states (i.e., a finite thickness spanned by a rarefaction fan). While the first and third peaks (*) are thought to be representative of the collection of (101) and (110) peaks during release, efforts to estimate c/a by fitting these peaks

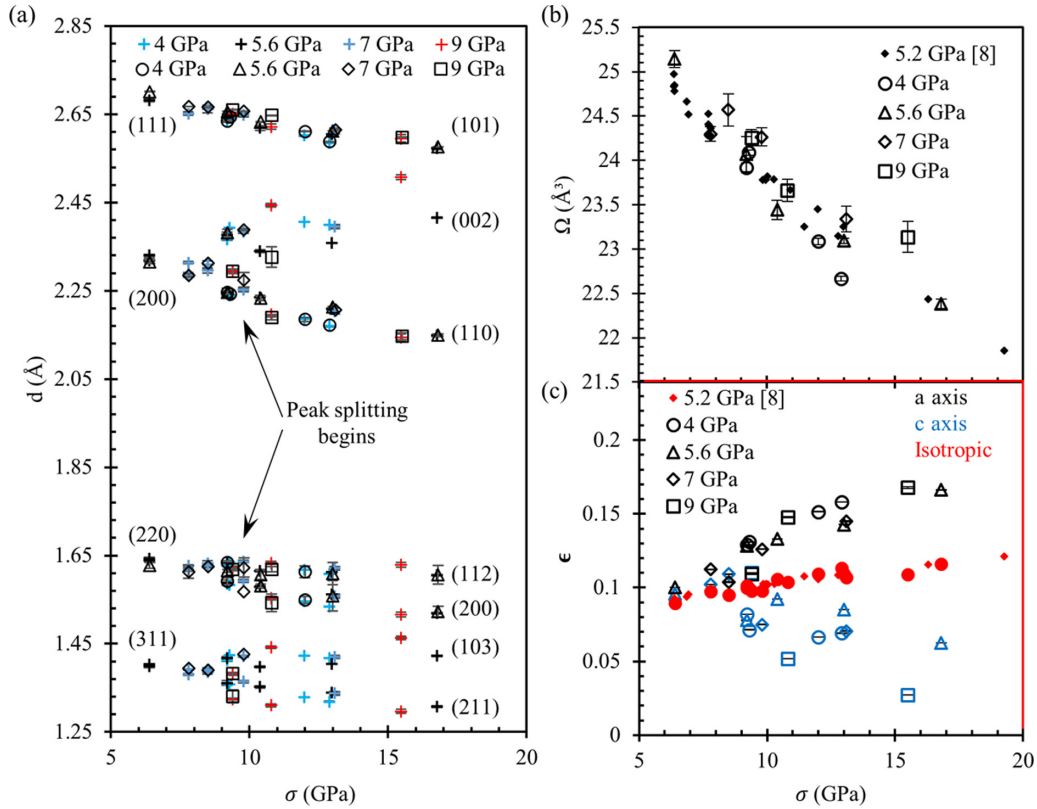

FIG. 7. (a) The measured d spacing (hollow black symbols) were used to constrain the values of c and a, with the d spacing corresponding to the fit lattice parameters (pluses) overlaid. (b) The measured atomic volume compares favorably with the volume along the 5.2 GPa secondary Hugoniot (filled diamonds) determined from measurements taken in [8]. (c) XRD provides a means of observing the linear strain along specific lattice directions. Note the difference between the linear strain assuming isotropic deformation versus what is experimentally observed, where the c axis actually expands relative to the first shock state.

yielded an unreasonably low value (nominally 1.3). The small peak between those diffraction peaks (m) is thought to be residual from the (101) peak at 16.8 GPa, and not representative of a released state. The final two diffraction patterns taken at 683 and 863 ns after breakout are of Ce following release to nominally ambient pressure. The diffraction patterns are consistent with fcc (γ-like) Ce at elevated temperature, and show no evidence of metastable ε-Ce, which would exhibit

TABLE II. Summary of parameters related to the fit *I*4/*mmm* unit cell.

Shot	σ_1 (GPa)	σ_2 (GPa)	a (Å)	c (Å)	c/a	Ω (Å^3)
19-4-045	4.68(24)	16.8(2)	3.042(3)	4.837(3)	1.590(2)	23.39(5)
19-4-046	5.41(44)	10.4(2)	3.164(7)	4.684(7)	1.481(4)	23.44(11)
19-4-047	5.84(75)	13.0 (4)	3.128(2)	4.721(2)	1.509(1)	23.09(3)
19-4-048	3.44(52)	12.0(1)	3.096(2)	4.817(2)	1.556(1)	23.09(4)
19-4-049	9.32(44)	15.5(3)	3.036(11)	5.020(11)	1.654(7)	23.14(18)
19-4-050	–	13.1(1)	3.120(9)	4.796(9)	1.537(5)	23.34(15)
19-4-051	3.46	9.3(1)	3.171(2)	4.791(1)	1.511(1)	24.09(3)
19-4-052	3.69	9.2(1)	3.177(4)	4.738(4)	1.491(2)	23.92(6)
19-4-053	2.61(43)	12.9(1)	3.072(2)	4.803(2)	1.564(1)	22.67(3)
21-4-016	6.47	9.2(2)	3.181(12)	4.758(12)	1.496(7)	24.07(20)
21-4-017	6.16	9.8(2)	3.189(6)	4.773(6)	1.497(4)	24.26(10)
21-4-018	7.38	8.5(3)	3.270(11)	4.597(11)	1.406(6)	24.57(18)
21-4-019	9.65	10.8(1)	3.250(4)	4.892(8)	1.573(5)	24.30(8)
19-4-004[a]	5.6	6.4(1)	3.283(6)	4.665(6)	1.421(6)	25.14(9)
19-4-006[a]	7.1	7.8(1)	3.250(6)	4.633(5)	1.431(3)	24.30(8)
19-4-007[a]	8.9	9.4(1)	3.283(6)	4.592(6)	1.413(3)	24.25(9)

[a]Diffraction data previously published in [1] refit assuming a bct structure.

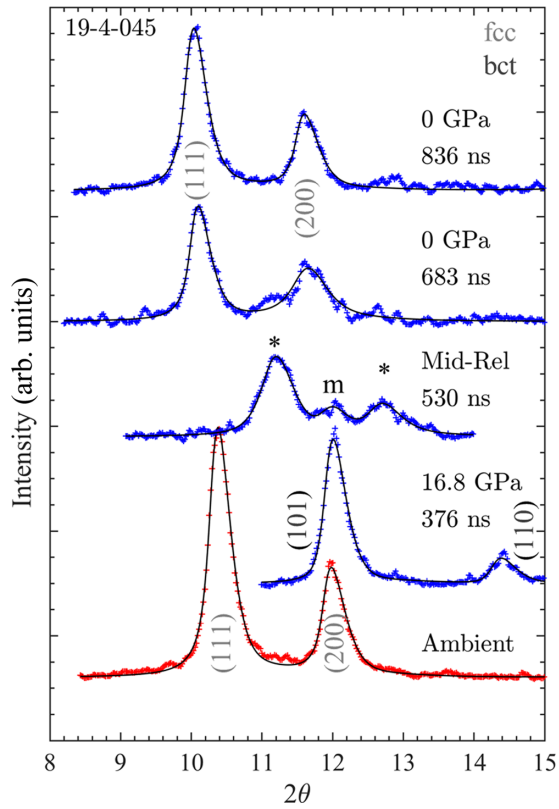

FIG. 8. Time-resolved diffraction of reversion from ε to fcc Ce. Symbols * and m are explained in the text. The time listed is relative to breakout of the first shock.

a larger separation between the observed peaks. The results show that reversion occurs rapidly, with no significant kinetic response.

IV. DISCUSSION

It is important to note that there is no region where fcc and bct peaks are observed to coexist under dynamic loading. Instead, the lattice is observed to distort from an fcc to a bct structure with steadily increasing c/a. This behavior is observable in total energy calculations of bct Ce with c/a equal to 1.5 and 1.65 referenced to the fcc structure [18], where the $c/a = 1.5$ bct structure becomes more stable than the fcc structure at higher volumes, but gives way to $c/a = 1.65$ at decreasing volumes. The experiments reported here suggest that c/a between the curves calculated in [18] are also accessible and smoothly become the most stable phase with increasing pressure along a given secondary Hugoniot. In this case, it is not clear whether it would be possible to discern where transition onset begins through continuum measurements.

In order to compare the results of Jensen *et al.* [8] with the diffraction measurements, Ω was determined from the reported σ, u_p, and shock velocities (U_s) along the 5.2 GPa secondary Hugoniot using the Rankine-Hugoniot jump conditions for multiple shocks [22]. In Fig. 7(b) it is shown that Ω measured through XRD agrees well with the value determined from the shock velocity measurements along the 5.2 GPa secondary Hugoniot, with the data following the ring up from 5.6 GPa agreeing within error through 17 GPa. Previously, the velocity of the second shock was used to justify a second phase forming by 12.25 GPa at 10 g/cm^3 (23.25 Å^3). This is observable as a slight discontinuity in the plot of σ-Ω; however, the results presented above show that by 12 GPa c/a has deviated significantly from the ideal fcc value of $\sqrt{2}$ (i.e., the transition has already occurred).

If the change in compressibility observed along the 5.2 GPa secondary Hugoniot does not indicate the onset of the α-ε phase transition, what then does it indicate? A possible explanation can be found in Fig. 7(c). This figure shows that ϵ_a (black triangles) steadily increases with σ for all of the observed states, while ϵ_c (blue triangles) decreases only slightly compared to the value at 5.6 GPa. Prior to 13 GPa, ϵ_c lies between 0.078 and 0.100 with the c axis expanding only slightly compared to the first shock state. Beyond 13 GPa, the c axis expands more rapidly with σ. This increase in the expansion of the c axis may be the cause of the change in compressibility and shock velocity beyond 12.25 GPa. Since the initial transition from an fcc-like c/a occurs without any obvious volume collapse, velocimetry based diagnostics do not observe the phase transition until the difference in compressibility becomes significant. However, the XRD measurements show that the transition begins prior to 9 GPa along the secondary Hugoniot centered at 5.6 GPA on the principal Hugoniot.

The evolution of c/a for the Ce α-ε phase transition has been a subject of several experimental and theoretical studies [9,14,15,18]. Figure 9 compares c/a measured in this work (hollow symbols) with previous static measurements (solid symbols) along the RT isotherm [14] and isotherms between 600 and 775 K [9]. At room temperature, interpretation of c/a is complicated by the transition to α' or α'' from 5 to 13 GPa. For the purposes of this discussion, an effective value of c/a is taken for the α' and α'' phases, as in [14,18]. Along the RT isotherm, c/a is initially $\sqrt{2}$ corresponding to an fcc structure (γ then α). Between 5 and 13 GPa, c/a is 1.52–1.55 corresponding to either α' or α''. By 13 GPa, where ε first appears along the RT isotherm, the c/a ratio transitions to 1.64 before gradually increasing with pressure and stabilizing at 1.68 above 50 GPa [15]. It is important to note that there are distinct jumps in c/a observed on transitions from α to α' (or α''), and then to ε. At temperatures above 600 K, c/a is observed to increase linearly from 1.43 to 1.48 from ~24.25 to 24 Å^3 with c/a decreasing with increasing temperature at a fixed Ω, Fig. 9(b). The available static data do not extend beyond $c/a = 1.5$ at temperatures above the α-ε-α'triple point and are limited by chemical reactions with increasing temperatures, which prevented measurement above 800 K [9].

Under dynamic conditions, a c/a between 1.435 and 1.48 is not observed, Fig. 9 (hollow symbols). It is possible that this is due to the narrow volume range over which the structure transitions from $\sqrt{2}$ to 1.48 in the static data (~0.25 Å^3); however, this does prevent extrapolation of c/a in Ω to determine the transition onset with the current dataset. The single observation of c/a ≈1.43 is thought to be indicative of the scatter in our measurements, since a lower c/a is observed at slightly higher stress along the same secondary

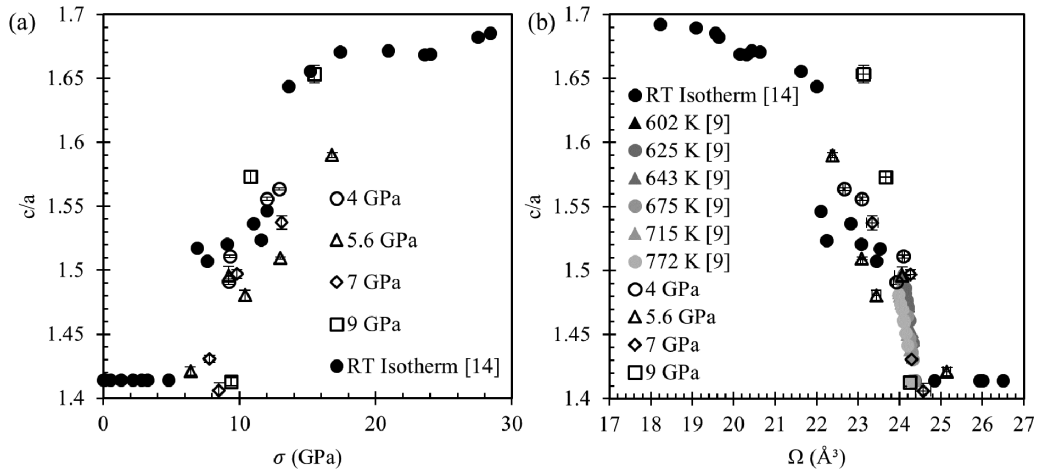

FIG. 9. Plots of the *c/a* ratio as a function of (a) σ and (b) Ω. Data collected under dynamic loading are plotted as hollow symbols, with data collected under static loading (Olsen *et al.* [14], Munro *et al.* [9]) are plotted as filled symbols. Note that when plotted as a function of atomic volume, the dynamic measurements tend to fall along a line extending from the end of Munro's static measurements to the beginning of Olsen's measurements in the bct phase near a *c/a* at 1.65.

Hugoniot, as well as at elevated stress along the principal Hugoniot. Following a rapid increase in *c/a* to ∼1.48, there is a steady increase in *c/a* with stress and density along a path extending from the maximum values reported by Munro *et al.* and the value observed when ε initially forms along the RT isotherm. The scatter in the data makes it difficult to definitively establish how *c/a* varies with temperature. It is noteworthy that the *c/a* observed along the secondary Hugoniot from 9 GPa (hollow squares) increase more rapidly with σ and are greater than what is observed at lower temperatures for a given Ω, despite the transition to ε occurring at higher σ compared to secondary from lower initial σ.

The transition from an ideal fcc *c/a* provides a means of constraining the α-ε phase boundary under dynamic loading. This transition occurs prior to 9 GPa along the 5.6 GPa secondary Hugoniot, between 8.5 and 9.2 GPa along the 7 GPa secondary Hugoniot, and between 9.4 and 10.8 GPa along the 9 GPa secondary Hugoniot. Since the volume change across the transition is either second order, with no transition enthalpy, or first order with a finite slope and negligibly small volume change (as evidenced by Munro et al. [9]) the temperature in the ε phase has been approximated by an α-EOS. Plotting the observed *c/a* ratios in *P-T* space reveals clear bounds on the location of the α-ε phase boundary, Fig. 10. A linear extension of these points anchored to the α-ε-α' triple point (6.14 GPa and 640 K [9])) intersects the melt boundary [13] near 11.5 GPa. While it is not clear that this is the α-ε-*L* triple point, this should serve as an approximate lower pressure limit for its location.

V. CONCLUSIONS

Dynamic experiments using XRD examining the high temperature solid region of the Ce phase diagram (5–18 GPa above 700 K) are reported, allowing the lattice spacing, atomic volume, linear strain, and the location of the α-ε phase boundary to be determined. The volume-stress relationship observed in this work compares favorably with a secondary Hugoniot reported previously [8]. However, the α-ε transition was found to begin prior to 12.25 GPa, where it was previously necessary to introduce a second EOS to explain measured shock velocities.

The α-ε transition is characterized by *c/a* deviating from $\sqrt{2}$ under dynamic loading. The reported results show a transition from $\sqrt{2}$ to ∼1.48 over small volume (∼0.25 Å^3) and pressure (1–2 GPa) ranges, before gradually increasing with increasing σ or Ω. While a steady value of *c/a* was not

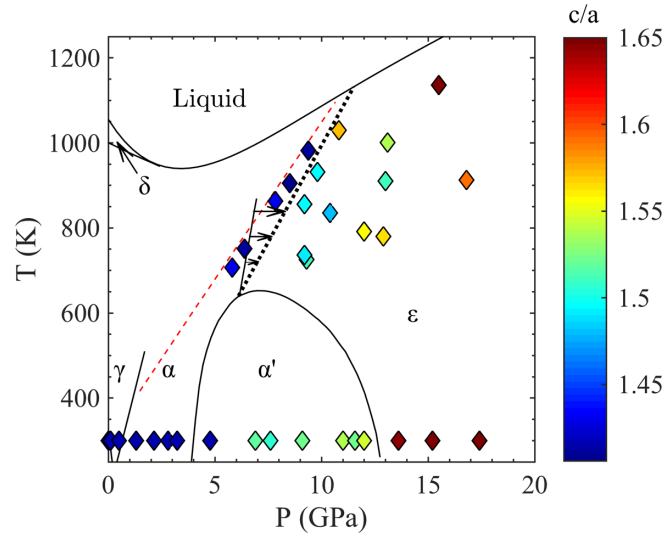

FIG. 10. The Ce *P-T* phase diagram with experimental data along the RT isotherm (Olsen *et al.* [14]) and dynamic experiments (including data from [1]) colored by the *c/a* ratio. The temperature under dynamic loading has been estimated using a multiphase equation of state with the behavior in the ε phase being approximated as α-Ce. Note that the observed boundary (black dotted line) is less steep than the boundary of Munro *et al.* [9], and does not intersect the solid Hugoniot.

established in this study, the maximum value observed (1.65) approaches the steady value observed in static experiments at high pressure (1.68) [15]. Cerium is found to remain in an fcc structure near the solid Hugoniot, despite intersecting previously reported static boundaries near 7 GPa [9,10]. The transition, as identified through c/a deviating from $\sqrt{2}$, is found to occur below the Hugoniot and does not intersect the Hugoniot in the solid phase. Using the states identified in this work along with the α-ε-α' triple point, the α-ε-L triple point is at or above 11.5 GPa.

On loading and release, the α-ε transition is observed to converge to a steady (over the timescale of these experiments) value of c/a. There is no evidence of an α-ε mixed region, where distinct regions of atoms arranged in an fcc orientation coexist with atoms arranged in a bct orientation. Instead, the uniform lattice suggests that fcc Ce rapidly transitions to a stable bct lattice. Since Ce melt kinetics [1] and α-ε transition kinetics (this work) have both been observed to be rapid through time-resolved XRD, it appears that the most likely explanation for the narrow melting range observed in pyrometry [2,11] along the Hugoniot is a small enthalpy of fusion, not slow transition kinetics.

ACKNOWLEDGMENTS

The authors would like to acknowledge Frank Cherne for providing *P-T* secondary Hugoniots and Joe Rivera for fabricating the targets and impactors used in this work. Los Alamos National Laboratory is operated by Triad National Security, LLC, for the national Nuclear Security Administration of the U.S. Department of Energy (Contract No. 89233218CNA000001). This paper is based upon work performed at the Dynamic Compression Sector, which is operated by Washington State University under the U.S. Department of Energy (DOE)/National Nuclear Security Administration Award No. DE-NA0003957. This research used resources of the Advanced Photon Source, a DOE Office of Science User Facility operated for the DOE Office of Science by Argonne National Laboratory under Contract No. DE-AC02-06CH11357.

[1] M. T. Beason, B. J. Jensen, and B. Branch, J. Appl. Phys. **128**, 165107 (2020).
[2] B. J. Jensen, T. M. Hartsfield, D. B. Holtkamp, F. J. Cherne, R. B. Corrow, T. E. Graves, and A. J. Iverson, Phys. Rev. B **102**, 214105 (2020).
[3] B. J. Jensen, F. J. Cherne, J. C. Cooley, M. V. Zhernokletov, and A. E. Kovalev, Phys. Rev. B **81**, 214109 (2010).
[4] A. Jayaraman, Phys. Rev. **137**, A179 (1965).
[5] V. M. Elkin, V. N. Mikhaylov, A. V. Petrovtsev, and F. J. Cherne, Phys. Rev. B **84**, 094120 (2011).
[6] B. J. Jensen and F. J. Cherne, J. Appl. Phys. **112**, 013515 (2012).
[7] M. J. Lipp, D. Jackson, H. Cynn, C. Aracne, W. J. Evans, and A. K. McMahan, Phys. Rev. Lett. **101**, 165703 (2008).
[8] B. J. Jensen, F. J. Cherne, and N. Velisavljevic, J. Appl. Phys. **127**, 095901 (2020).
[9] K. A. Munro, D. Daisenberger, S. G. MacLeod, S. McGuire, I. Loa, C. Popescu, P. Botella, D. Errandonea, and M. I. McMahon, J. Phys.: Condens. Matter **32**, 335401 (2020).
[10] A. Schiwek, F. Porsch, and W. B. Holzapfel, High Pressure Res. **22**, 407 (2010).
[11] R. Hixson, B. La Lone, M. Staska, G. Stevens, W. Turley, and L. Veeser, J. Appl. Phys. **129**, 155106 (2021).
[12] C. T. Seagle, M. P. Desjarlais, A. J. Porwitzky, and B. J. Jensen, Phys. Rev. B **102**, 054102 (2020).
[13] B. Sitaud, J. Péré, and T. Thévenin, High Pressure Res. **12**, 175 (1994).
[14] J. S. Olsen, L. Gerward, U. Benedict, and J.-P. Itié, Physica B+C (Amsterdam) **133**, 129 (1985).
[15] Y. K. Vohra, S. L. Beaver, J. Akella, C. A. Ruddle, and S. T. Weir, J. Appl. Phys. **85**, 2451 (1999).
[16] O. Tsiok and L. Khvostantsev, J. Exp. Theor. Phys. **93**, 1245 (2001).
[17] Y. Zhao and W. Holzapfel, J. Alloys Compd. **246**, 216 (1997).
[18] P. Soderlind, Adv. Phys. **47**, 959 (1998).
[19] J. W. Allen and R. M. Martin, Phys. Rev. Lett. **49**, 1106 (1982).
[20] F. Decremps, L. Belhadi, D. L. Farber, K. T. Moore, F. Occelli, M. Gauthier, A. Polian, D. Antonangeli, C. M. Aracne-Ruddle, and B. Amadon, Phys. Rev. Lett. **106**, 065701 (2011).
[21] K. Momma and F. Izumi, J. Appl. Crystallogr. **44**, 1272 (2011).
[22] J. W. Forbes, *Shock Wave Compression of Condensed Matter: A Primer* (Springer Science & Business Media, Berlin, 2013).
[23] B. J. Jensen, D. B. Holtkamp, P. A. Rigg, and D. H. Dolan, J. Appl. Phys. **101**, 013523 (2007).
[24] N. Sinclair, S. Turneaure, Y. Wang, K. Zimmerman, and Y. Gupta, J. Synchrotron Radiat. **28**, 1216 (2021).
[25] B. H. Toby and R. B. Von Dreele, J. Appl. Crystallogr. **46**, 544 (2013).
[26] S. P. Marsh, *LASL Shock Hugoniot Data* (University of California Press, Berkeley, 1980), Vol. 5.
[27] D. R. Jones, B. M. Morrow, C. P. Trujillo, G. T. Gray III, and E. K. Cerreta, J. Appl. Phys. **122**, 045902 (2017).
[28] S. Song and G. Gray III, Philos. Mag. A **71**, 275 (1995).
[29] B. J. Jensen, G. T. Gray, and R. S. Hixson, J. Appl. Phys. **105**, 103502 (2009).